Triplet pair density wave superconductivity on the π-flux square lattice

Daniel Shaffer and Luiz H. Santos
Department of Physics, Emory University, 400 Dowman Drive, Atlanta, Georgia 30322, USA

(Received 5 November 2022; revised 16 June 2023; accepted 26 June 2023; published 18 July 2023)

Pair-density waves (PDWs) are superconducting states that spontaneously break translation symmetry in systems with time-reversal symmetry (TRS). Evidence for PDWs has been seen in several recent experiments, as well as in the pseudogap regime in cuprates. Theoretical understanding of PDWs has been largely restricted to phenomenological and numerical studies, while microscopic theories typically require strong coupling or fine tuning. In this work, we provide a symmetry-based mechanism under which PDWs emerge as a weak-coupling instability of a two-dimensional TRS metal. Combining mean-field and renormalization-group analyses, we identify a weak-coupling instability towards a triplet PDW realized in the π-flux square lattice model with on-site repulsion and moderate nearest-neighbor attraction when the Fermi level crosses Van Hove singularities at $1/4$ and $3/4$ fillings. This PDW is protected by the magnetic translation symmetries characteristic of Hofstadter systems, of which the π-flux lattice is a special time-reversal-symmetric case.

DOI: 10.1103/PhysRevB.108.035135

I. INTRODUCTION

Several recent experiments on different materials, including cuprates [1,2], transition-metal dichalcogenides [3], kagome systems [4], and most recently UTe_2 [5,6], have reported an exotic form of spatially nonuniform superconductivity called a pair-density wave (PDW) [7]. Unlike the similar Fulde–Ferrell–Larkin–Ovchinnikov (FFLO) states, PDWs descend from a time-reversal invariant normal state. On the theory side, however, it has been a great challenge to identify scenarios where such elusive order can form. Apart from one-dimensional (1D) systems [8–13], most of the few microscopic mechanisms for PDW that have been proposed generally require strong coupling [14–22].

The main obstacle to the weak-coupling theory, which would otherwise be desirable, is that the logarithmic divergence of the pairing susceptibility $\Pi_{\boldsymbol{Q}}$ indicating the formation of Cooper pairs with finite center-of-mass $\boldsymbol{Q}$ generally only occurs at $\mathbf{Q} = 0$ and no other momentum, leading only to uniform superconductivity (SC). The divergence is a consequence of the degeneracy of single-particle states $\varepsilon_{\boldsymbol{k}} = \varepsilon_{-\boldsymbol{k}}$, which is guaranteed by either time-reversal or inversion symmetry. In the few weak-coupling theories for PDWs that have been proposed recently [23–30], this issue is circumvented by identifying Fermi surfaces that satisfy a PDW nesting condition $\varepsilon_{\boldsymbol{k}} = \varepsilon_{-\boldsymbol{k}+\boldsymbol{Q}}$, which leads to the desired logarithmic divergence of $\Pi_{\boldsymbol{Q}}$. However, the nesting condition in all these models is in general accidental and therefore requires some degree of fine tuning.

In this work, we show that the PDW nesting condition is satisfied by symmetry without any fine-tuning in the two-dimensional (2D) π-flux square lattice model, a special case of the Hofstadter model [31] that preserves time-reversal symmetry (it is thus also a special case of the TR-symmetric Hofstadter model [32]). The relevant symmetry is a magnetic translation symmetry (MTS) that acts as sublattice symmetry in real space and as a translation by $\boldsymbol{Q} = (0, \pi)$ in the magnetic Brillouin zone (BZ), which guarantees the nesting condition $\varepsilon_{\boldsymbol{k}} = \varepsilon_{-\boldsymbol{k}+\boldsymbol{Q}}$. The reconstruction of the Fermi surface due the large π-flux per unit cell thus enables Cooper pairing with finite momentum [33], stabilizing a new class of (magnetic-translation) symmetry-protected PDWs.

The focus of earlier studies on the π-flux lattice has been on Dirac fermions at half filling, notably (but not exclusively) in the context of flux phases in cuprates [34–36], quantum Hall transitions [37], electron fractionalization [38–40] in 2D lattices, and uniform SC and charge-density wave (CDW) instabilities [41,42]. Here we instead consider the Van Hove singularities (VHS) of this system that occur at the less explored $1/4$ and $3/4$ fillings as the driving microscopic mechanism of the PDW instability. At the VHS the Fermi surfaces have an addition nesting in the spin-density wave (SDW) channel, which together with diverging density of states (DOS) near the VHSs enhances spin fluctuations that open the door to unconventional electronic pairing [43], recently shown to lead to uniform singlet d-wave-like superconductor driven by on-site repulsive Hubbard interaction in the π-flux lattice [44].

Our main result is the identification of a weak-coupling instability towards a triplet PDW ground state in the π-flux lattice when moderate nearest neighbor attractive interactions are added to the onsite repulsive Hubbard interaction. We establish the existence of the PDW state using mean-field theory and confirm its stability with renormalization group (RG) methods that rule out alternative competing phases (SC, CDW, and SDW), while also establishing the stability of the PDW against small detuning from perfect nesting in the SDW channel which, in contrast to the PDW nesting, can occur due to symmetry-allowed perturbations. The MTS-protected triplet PDW represents a new class of unconventional pairing that is of particular interest in light of the realization of Hofstadter bands in moiré lattices [45–49] and recent experimental advances towards their realization using synthetic gauge fields in optical lattices [50–52]. The recently fabricated twisted

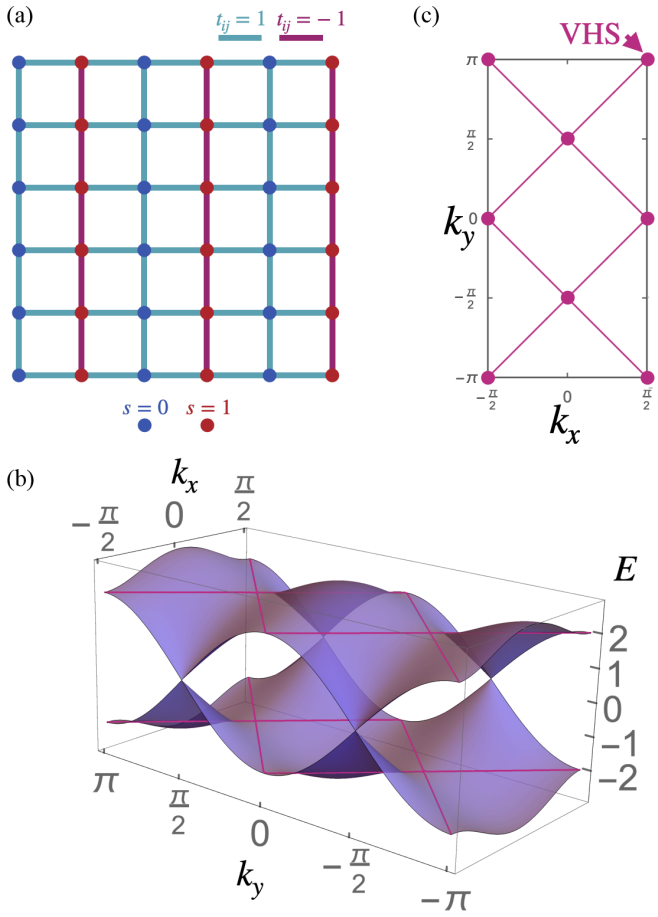

FIG. 1. (a) The square π-flux lattice. Sublattices marked as blue ($s = 0$) and red ($s = 1$). (b) The two bands of the π-flux lattice dispersion defined on the MBZ. There are two Dirac nodes on the MBZ boundary at $\pm(\pi/2, \pi/2)$. (c) Fermi surface and VHS in the MBZ.

double-layer copper-oxides are another promising platform where the π-flux model may be relevant [53,54].

II. THE π-FLUX LATTICE MODEL

The π-flux square lattice Hamiltonian is

$$H_0 = -t \sum_{\langle \mathbf{r}\mathbf{r}'\rangle\sigma} (-1)^{(r_y - r'_y)r_x} c^\dagger_{\mathbf{r}\sigma} c_{\mathbf{r}'\sigma} + \text{H.c.} - \mu \sum_{\mathbf{r}\sigma} c^\dagger_{\mathbf{r}\sigma} c_{\mathbf{r}\sigma}, \tag{1}$$

where $c_{\mathbf{r}\sigma}$ are fermion annihilation operators at site $\mathbf{r}$ of the square lattice with spin $\sigma = \uparrow, \downarrow$, t is the nearest-neighbor hopping amplitude that we set to 1, and μ is the chemical potential. We take r_x, r_y to be integer multiples of the lattice constant $a = 1$ and consider $\mu = \pm 2t$ corresponding to energy of the VHSs. See Fig. 1(a).

The symmetries of the π-flux model will play an important role in our analysis below. H_0 possesses TRS and inversion symmetry, as well as magnetic translation symmetries $\hat{T}_y = T_y$ and $\hat{T}_x = (-1)^{r_y} T_x$ generating the magnetic translation group (MTG), where T_x and T_y are ordinary lattice translations. In particular, the translation T_x is broken by H_0, so that there are two sites per unit cell along the x direction which we label with a sublattice index $s = 0, 1$ as shown in Fig. 1(a). In addition, H_0 has a fourfold magnetic rotation symmetry $\hat{C}_4 = (-1)^{r_x r_y} C_4$ which is a combination of the regular C_4 symmetry with a gauge transformation that correspondingly rotates the magnetic vector potential; see Appendix A (other crystalline symmetries of the square lattice have similar magnetic versions).

H_0 is partially diagonalized by the momentum-space operators $c_{\mathbf{k}s\sigma} = \frac{1}{\sqrt{N}} \sum_{\mathbf{R}} e^{-i\mathbf{k}\cdot(s\hat{\mathbf{x}}+\mathbf{R})} c_{s\hat{\mathbf{x}}+\mathbf{R},\sigma}$ where $\mathbf{R}$ defines the lattice with the extended unit cell and N is the number of extended sites. The momentum $\mathbf{k}$ is thus restricted to the magnetic Brillouin zone (MBZ) with $k_y \in (-\pi, \pi]$ and $k_x \in [-\pi/2, \pi/2]$, such that the original Brillouin zone (BZ) is folded along the k_x direction [see Figs. 1(b) and 1(c)]. In momentum space, the single-body Hamiltonian can be written as $H_0 = \sum_{\mathbf{k}\sigma} \mathbf{c}^\dagger_{\mathbf{k}\sigma} \mathcal{H}_0(\mathbf{k}) \mathbf{c}_{\mathbf{k}\sigma}$ where $\mathbf{c}_{\mathbf{k}\sigma} = (c_{\mathbf{k},0,\sigma}, c_{\mathbf{k},1,\sigma})^T$ and $\mathcal{H}_0(\boldsymbol{k}) = 2t \cos k_x \tau^x - 2t \cos k_y \tau^z - \mu$, with τ^j being Pauli matrices acting on sublattice indices. $\mathcal{H}_0(\mathbf{k})$ is diagonalized by operators

$$d_{\mathbf{k}\alpha\sigma} = \sum_s \frac{\alpha^s}{\sqrt{2}} \sqrt{1 + \alpha(-1)^s \frac{\cos k_y}{E(\mathbf{k})}}\, c_{\mathbf{k}s\sigma}, \tag{2}$$

where $E(\mathbf{k}) = (\cos^2 k_x + \cos^2 k_y)^{1/2}$ and $\alpha = \pm 1$ labels the Hofstadter bands with energies $\epsilon_\alpha(\mathbf{p}) = 2t\alpha E(\mathbf{k}) - \mu$. The two bands meet at zero energy at two Dirac nodes located at the MBZ boundary at $\mathbf{k} = \pm(\pi/2, \pi/2)$, see Fig. 1(b). In this work we investigate electronic states near 1/4 and 3/4 fillings at which the bottom and top bands, respectively, have four VHSs, as shown in Fig. 1(c).

Extended Hubbard interactions and irreducible representations. To investigate interaction effects, we add to Eq. (1) an extended Hubbard interaction:

$$H_I = U \sum_{\mathbf{r}} n_{\mathbf{r}\uparrow} n_{\mathbf{r}\downarrow} + V \sum_{\langle \mathbf{r}\mathbf{r}'\rangle\sigma\sigma'} n_{\mathbf{r}\sigma} n_{\mathbf{r}'\sigma'}, \tag{3}$$

where $n_{\mathbf{r}\sigma} = c^\dagger_{\mathbf{r}\sigma} c_{\mathbf{r}\sigma}$ is the electron-density operator, and U and V are the on-site and nearest-neighbor density-density interaction strengths, respectively. We consider both positive (repulsive) and negative (attractive) values of U and V. Following the approach in Ref. [44], we project the interactions onto the Hofstadter band α crossing the chemical potential tuned to the VHS. This is done by replacing the $c_{\mathbf{r}\sigma}$ operators in Eq. (3) with the band basis $d_{\mathbf{k}\alpha}$ operators from Eq. (2), and restricting the α index to a single value.

We further decompose the interactions into pairing channels corresponding to the different irreducible representations (irreps) of the symmetries of the π-flux lattice. The relevant irreps of the MTG symmetries for arbitrary rational flux have been classified in Ref. [33]. The key observation for constructing the irreps is that the operator $\hat{T}_x \hat{T}_y \hat{T}_x^{-1} \hat{T}_y^{-1}$ corresponding to a loop operator going around a single unit cell of the square lattice is a $U(1)$ transformation under which the electrons pick up an Aharonov-Bohm phase equal to the encircled flux, a phase of π on the π-flux lattice. A *pair* of electrons, on the other hand, picks up a trivial phase, such that the action of $\hat{T}_x$ and $\hat{T}_y$ on the pairing gap function commutes. As a result, we can classify the gap functions according to it being even or odd under the MTG symmetries, with all four combinations being possible. These correspond to four one-dimensional irreps of

the MTG that we label (ℓ_x, ℓ_y) with $\ell_j = 0, 1$ corresponding to Cooper pairs with momenta $\pi(\ell_x, \ell_y)$ and picking up a phase of $(-1)^{\ell_j}$ under $\hat{T}_j$. The uniform SC state corresponds to $\ell_x = \ell_y = 0$, and the other three irreps are PDW orders.

In addition, the electrons can form either singlet or triplet pairs [the irreps of spin rotation symmetry, unbroken by the spin-conserving interactions Eq. (3)]. We thus label the gap functions as $\Delta^{(\ell_x\ell_y\nu)}$, with $\nu = 0$ corresponding to singlet and $\nu = x, y, z$ corresponding to the three triplet components. Finally, when $\ell_x = \ell_y$, the Cooper pair momentum is invariant under $\hat{C}_4$ and the gap function can thus be even or odd under $\hat{C}_4$, which we refer to as s-wave or d-wave pairing respectively and label the corresponding gap functions as $\Delta^{(\ell_x\ell_y\nu;s)}$ and $\Delta^{(\ell_x\ell_y\nu;d)}$. When $\ell_x \neq \ell_y$, since $\hat{C}_4$ interchanges the action of $\hat{T}_x$ and $\hat{T}_y$, the gap functions necessarily break the $\hat{C}_4$ symmetry, implying that there are at least two degenerate ground states of the system. In particular, $\Delta^{(01\nu)}$ and $\Delta^{(10\nu)}$, which correspond to pairs with total momenta $\bar{\mathbf{Q}} = (\pi, 0)$ and $\mathbf{Q} = (0, \pi)$, respectively, are mapped to each other under $\hat{C}_4$. This means that although they form two 1D irreps of the MTG taken separately [33], taken together they form two components of a 2D irrep of the MTG combined with $\hat{C}_4$.

The crystalline symmetry relations above determine the space group irreps describing the PDW order parameters [55], which are direct products of the irrep of the little point group (the subgroup of the point group that keeps the total momentum of the pair fixed) and the star of the total momentum of the pair (i.e., the collection of all momenta mapped to each other by the point-group symmetries). All the irreps and representative gap functions are summarized in Table I, with the relevant little point groups being the trivial group for channels with the star $\mathbf{Q}^* = \{\mathbf{Q}, \bar{\mathbf{Q}}\}$ and C_{4h} otherwise (the smallest point group containing inversion and $\hat{C}_4$ symmetry).

Having identified the irreps, the interactions projected onto the band α can be decomposed into the corresponding channels as

$$H^{(\ell_x\ell_y\nu)}_{int,\alpha} = \frac{1}{2}\sum_{\substack{\mathbf{kp}\sigma_1\sigma_1'\\ \sigma_2\sigma_2'}} g^{(\ell_x\ell_y\nu)}(\mathbf{p};\mathbf{k})(\sigma^\nu i\sigma^y)^*_{\sigma_1\sigma_1'}(\sigma^\nu i\sigma^y)_{\sigma_2\sigma_2'} \times d^\dagger_{\mathbf{p}+\ell_x\mathbf{Q},\alpha\sigma_1} d^\dagger_{-\mathbf{p}\alpha\sigma_1'} d_{-\mathbf{k}\alpha\sigma_2} d_{\mathbf{k}+\ell_x\mathbf{Q},\alpha\sigma_2'}, \quad (4)$$

where $g^{(\ell_x\ell_y\nu)}(\mathbf{p};\mathbf{k}) = \sum_m g^{(\ell_x\ell_y\nu)}_m \Phi^{(\ell_x\ell_y\nu)}_m(\mathbf{p})\Phi^{(\ell_x\ell_y\nu)}_m(\mathbf{k})$ with $g^{(\ell_x\ell_y\nu)}_m$ being the coupling *constants*, $m = 0, 1, \ldots$ labeling terms belonging to the same irrep and $\Phi^{(\ell_x\ell_y\nu)}_m(\mathbf{p})$ being basis functions; $g^{(\ell_x\ell_y\nu)}_m$ and $\Phi^{(\ell_x\ell_y\nu)}_m(\mathbf{p})$ obtained from the extended Hubbard interactions are summarized in Table I. Note that the projections in this case do not depend on the band index α, which we therefore henceforth omit.

TABLE I. Basis functions $\Phi^{(\ell_x\ell_y\nu)}_m(\mathbf{k})$ for gap functions and interactions arising in the extended Hubbard model. First column: space group irrep composed of the little point-group irrep times the star of the momentum of the order. If only the point group is shown, the momentum star is trivial. The nontrivial momentum star is $\mathbf{Q}^* = \{(0,\pi),(\pi,0)\}$, for which the little point group is trivial. We label the momentum star $\mathbf{Q}^*_s$ and $\mathbf{Q}^*_t$ to distinguish singlet and triplet channels. The second column shows $(\ell_x\ell_y\nu)$ labels defined in the main text. Third column: $\Phi^{(\ell_x\ell_y\nu)}_m(\mathbf{k})$, with multiple rows in a single channel corresponding to different values of m, meaning either several functions belong to the same 1D irrep or they from two components of the 2D irreps. Fourth column: coupling constants giving rise to the corresponding channels, with leading channels shown as boxed.

Space group irrep	$(\ell_x\ell_y\nu)$	$\Phi^{(\ell_x\ell_y\nu)}_m(\mathbf{k})$	$g^{(\ell_x\ell_y\nu)}_m$
$\boxed{A_g}$	$(00s;s)$	1	$U/2$
		$(\cos^2 k_y + \cos^2 k_x)/E(\mathbf{k})$	V
$\boxed{B_g}$	$(00s;d)$	$(\cos^2 k_y - \cos^2 k_x)/E(\mathbf{k})$	V
$\mathbf{Q}^*_s$	$(01s)$	$\cos k_y/E(\mathbf{k})$	$U/2$
		$\cos k_y$	V
	$(10s)$	$\cos k_x/E(\mathbf{k})$	$U/2$
		$\cos k_x$	V
E_g	$(10s)$	$\sin k_y \cos k_x/E(\mathbf{k})$	V
		$\sin k_x \cos k_y/E(\mathbf{k})$	V
E_u	$(00t)$	$\sin k_y \cos k_y/E(\mathbf{k})$	V
		$\sin k_x \cos k_x/E(\mathbf{k})$	V
$\boxed{\mathbf{Q}^*_t}$	$(01t)$	$\sin k_y$	V
	$(10t)$	$\sin k_x$	V
A_u	$(11t)$	$\cos k_x \cos k_y/E(\mathbf{k})$	V

III. MEAN-FIELD ANALYSIS

The mean-field pairing Hamiltonian reads

$$H_\Delta = \sum_{\ell_x\nu\mathbf{p}} \Delta^{(\ell_x\nu)}(\mathbf{p})(\sigma^\nu i\sigma^y)_{\sigma\sigma'} d^\dagger_{\mathbf{p}+\ell_x\mathbf{Q},\sigma} d^\dagger_{-\mathbf{p}\sigma'} + \text{H.c.}, \quad (5)$$

with $\Delta^{(\ell_x\nu)}(\mathbf{p})$ being the gap functions, which, near the phase transition at the critical temperature T_c, satisfy the linearized gap equation $\Delta^{(\ell_x\nu)}(\mathbf{p}) = -\sum_{\ell_y,\mathbf{k}} g^{(\ell_x\ell_y\nu)}(\mathbf{p};\mathbf{k})\Pi_{\ell_x\mathbf{Q}}(\mathbf{k})\Delta^{(\ell_x\nu)}(\mathbf{k})$ where $\Pi_{\ell_x\mathbf{Q}}(\mathbf{k}) = \tanh(\frac{\epsilon_\alpha(\mathbf{k})}{2T})/\epsilon_\alpha(\mathbf{k})$ is the pairing susceptibility. Observe that the susceptibility has a logarithmic divergence and is independent of ℓ_x, which is a direct consequence of the $\hat{T}_x$ symmetry that identifies states at $\mathbf{k}$ and $\mathbf{k}+\mathbf{Q}$. We emphasize that this means that the weak-coupling PDW instability is symmetry protected in the π-flux model along with the usual uniform SC instability.

The solutions of the linearized gap equation take the form $\Delta^{(\ell_x\ell_y\nu)}(\mathbf{p}) = \sum_m D^{(\ell_x\ell_y\nu)}_m \Phi^{(\ell_x\ell_y\nu)}_m(\mathbf{p})$ where $D^{(\ell_x\ell_y\nu)}_m$ are coefficients satisfying $D^{(\ell_x\ell_y\nu)}_m = -\sum_{m'} g^{(\ell_x\ell_y\nu)}_{m'} \tilde{\Pi}^{(\ell_x\ell_y\nu)}_{mm'} D^{(\ell_x\ell_y\nu)}_{m'}$ (see Appendix B). This is a matrix equation with $\tilde{\Pi}^{(\ell_x\ell_y\nu)}_{mm'} = \sum_{\mathbf{k}} \Pi_0(\mathbf{k})\Phi^{(\ell_x\ell_y\mu)}_m(\mathbf{k})\Phi^{(\ell_x\ell_y\nu)}_{m'}(\mathbf{k})$. We solve this equation numerically to obtain the phase diagram shown in Fig. 2(a). The mean-field analysis uncovers three regimes. When both U and V are positive, i.e., there are only repulsive interactions, we find that there is no pairing instability, so the system remains a metal. For negative (attractive) U, the $(00s;s)$ uniform SC channel in the A_g irrep always has the highest T_c irrespective of the sign of V. However, an interesting situation arises for positive U and negative (attractive) V, where we identify the triplet PDW channels $(01t)$ and $(10t)$ as the leading

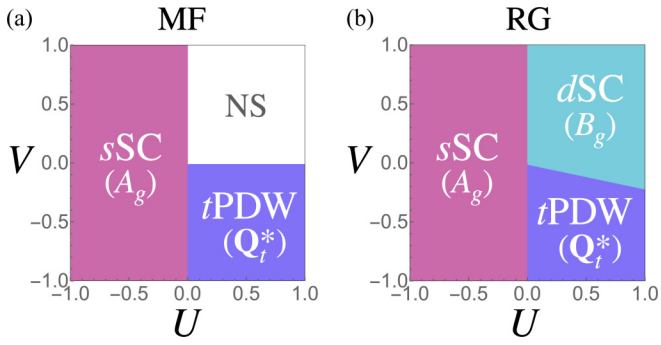

FIG. 2. Phase diagrams for the square π-flux lattice with extended Hubbard interactions in the parameter space of U (on-site) and V (nearest-neighbor) density-density interaction strengths (units are arbitrary), obtained using (a) mean-field and (b) patch RG calculations. In both cases on-site attraction ($U < 0$) results in a uniform s-wave SC belonging to the A_g irrep in Table I, while nearest-neighbor attraction with on-site repulsion ($V < 0$, $U > 0$) results in a triplet PDW in the $\mathbf{Q}_t^*$ irrep in Table I. In the latter case nodal unidirectional and fully gapped bidirectional PDW ground states are degenerate. The difference in the RG analysis is that a d-wave uniform SC phase in the B_g irrep is realized even when all interactions are repulsive, as well as for $-0.21U < V < 0$, whereas in mean field the system stays in the normal state (NS).

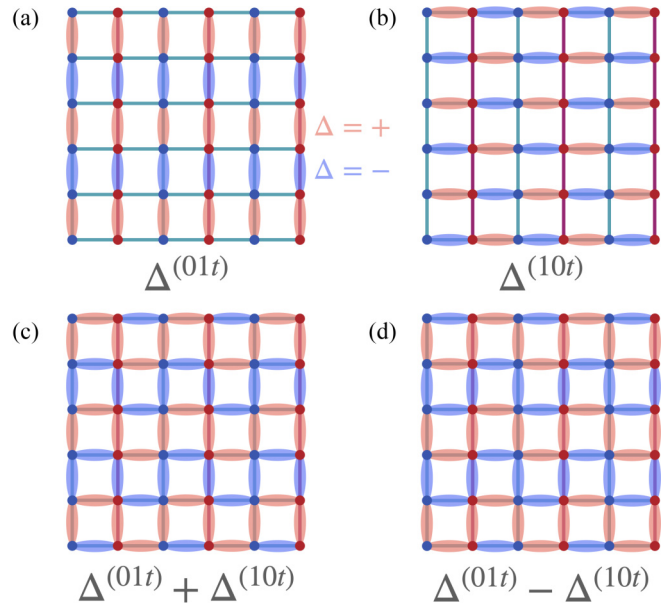

FIG. 3. Triplet PDW order parameters in real space obtained from minimizing the fourth-order free energy (6). Panels (a) and (b) show the two nodal unidirectional PDW phases, $\Delta^{(01t)}$ and $\Delta^{(10t)}$ respectively. Panels (c) and (d) show the two fully gapped bidirectional PDW phases that are linear combinations of the nodal phases.

instabilities with the same highest T_c. That is, the two solutions are degenerate and form two components of the 2D irrep $\mathbf{Q}_t^*$ of the space group, being mapped to each other by the $\hat{C}_4$ symmetry. This means that any linear combination of the solutions $\Delta^{(01t)}$ and $\Delta^{(10t)}$ satisfy the linearized gap equation.

This degeneracy is lifted by the fourth-order terms in the free energy, which in our case is similar to the one considered in Ref. [56]. Within our model, we compute the fourth-order term to be (omitting the $\nu = t$ index for clarity)

$$\mathcal{F}^{(4)} = \beta_0(|D^{(01)}|^2 + |D^{(10)}|^2)^2 + 2\beta_1|D^{(01)}|^2|D^{(10)}|^2 - \beta_1[(D^{(01)}D^{(10)*})^2 + \text{c.c.}]. \quad (6)$$

with $\beta_0, \beta_1 > 0$ (see Appendix C). The free energy is symmetric under $\hat{C}_4$ that takes $D^{(01)} \to D^{(10)} \to -D^{(01)}$. The minimum of the free energy is degenerate between a unidirectional PDW in which only one of $D^{(01)}$ or $D^{(10)}$ is nonzero (breaking the $\hat{C}_4$ symmetry), and bidirectional combinations with $D^{(01)} = \pm D^{(10)}$; in both cases TRS is preserved. Additional terms neglected in our model may favor either the unidirectional or bidirectional combinations. See Fig. 3 that shows the corresponding real-space order parameters. The triplet PDW gap functions have the form $\Delta^{(01t)} \propto \sin p_y$ and $\Delta^{(10t)} \propto \sin p_x$, resulting in a nodal fermionic excitation spectrum in the unidirectional phase, but a fully gapped spectrum in the bidirectional case. Note that, for the $\ell_x = 1$ unidirectional and the bidirectional phases, the MBZ is further folded along the p_y direction, with $p_y \in (-\pi/2, \pi/2]$. Although $\hat{T}_x$ is broken in that case, the ground states still have a $\mathbb{Z}_2$ symmetry that is a combination of MTG symmetries and a $U(1)$ transformation, resulting in a twofold degenerate excitation spectrum.

IV. RENORMALIZATION GROUP ANALYSIS

A limitation of the self-consistent mean-field analysis is that it does not consider all possible instabilities of the system, including possible charge (CDW) and spin-density wave (SDW) instabilities. To confirm that the phases found above are true ground states of the system we therefore carry out an additional patch RG analysis following [44] that extended the standard VHS patch RG framework used in the context of cuprates [57,58] and doped graphene [59] to the Hofstadter-Hubbard model with on-site interactions. Here we use the same framework extended to include nearest-neighbor interactions (see Appendix D).

In this framework we consider the values of the gap functions and the interactions only in the vicinity of the saddle points that give rise to the VHS (see Fig. 1), since the density of states diverges at these points. As a result the patch RG has a limitation in juxtaposition to the mean-field analysis as it only determines the gap function at the VHS points. As one consequence, we find that in RG the triplet PDW channel is further degenerate with the $(11s)$ singlet PDW that is odd with respect to both $\hat{T}_x$ and $\hat{T}_y$, and further transforms as a 2D irrep E_g of the point group. However, the mean-field analysis shows that this degeneracy is lifted already at the level of the linearized gap equation in favor of the triplet PDW channel. The two methods therefore complement each other.

The resulting RG phase diagram is shown in Fig. 2(b). The main difference from the mean-field phase diagram is the appearance of a d-wave $(00s; d)$ uniform SC channel belonging to the B_g irrep when all interactions are repulsive, consistent with the results in Ref. [44]. The d-wave SC moreover competes with the triplet PDW phase for negative V, but the PDW remains the winning instability as long as $0.21U < -V$,

within numerical accuracy. We verified that imperfect nesting in the SDW channel, which can occur due to additional hopping terms or slight shifts in the chemical potential, does not significantly alter the phase diagram. Importantly, the RG analysis rules out the CDW and SDW instabilities and establishes that the triplet PDW is indeed the leading instability in a large portion of the phase diagram.

V. DISCUSSION

In this work we showed that a symmetry-protected triplet PDW is realized at weak-coupling in the π-flux lattice with repulsive on-site interactions and moderate nearest-neighbor attraction. The symmetries that protect this PDW are the magnetic translation symmetries that are characteristic of Hofstadter systems. In particular, the triplet PDW is therefore robust to any perturbations that do not break these symmetries, including additional hopping terms, small shifts in the chemical potential, etc. As any logarithmic instability, it is also reasonably robust against perturbations that do break some of these symmetries, such as translation-symmetry disorder, as long the symmetry breaking is weak; in such cases the critical temperature will most likely be reduced, but the PDW phase will not be immediately destroyed as long as the energy scale of the perturbation (e.g., inverse scattering time τ^{-1} for disorder) is small compared with T_c computed in the absence of the perturbation. We emphasize that the robustness of the triplet PDW is due to the presence of the symmetry protected logarithm in the pairing susceptibility, which is absent in earlier weak-coupling theories of PDWs where the logarithm is not protected by any symmetry.

This finding opens interesting new research directions to pursue other phenomena that emerge from PDW states. For instance, it will be important to investigate the nature of induced, vestigial, and intertwined orders associated with this new triplet PDW phase, and to draw comparisons with the class of PDW states introduced as a way to explain cuprate phase diagrams [7,60]. These can interact in nontrivial ways with PDW vortices which may be fractional [56] or give rise to exotic charge-4e condensates [61]. Extensions of the present model may uncover mechanisms that lift the degeneracy between the gapless unidirectional and gapped bidirectional PDWs, which may include disorder or effects associated with the gapless fermionic excitations that may be gapped out by additional interactions [62]. We leave these open questions for future studies.

ACKNOWLEDGMENTS

We thank Jian Wang for useful discussions and earlier collaborations. This research is supported by the U.S. Department of Energy, Office of Science, Basic Energy Sciences, under Award No. DE-SC0023327 and by startup funds at Emory University.

APPENDIX A: INTERACTION PROJECTIONS

Here we go over some details of the projection of the interactions in Eq. (3). In momentum space in the sublattice basis

$$c_{\mathbf{k}s\sigma} = \frac{1}{\sqrt{N}} \sum_{\mathbf{R}} e^{-i\mathbf{k}\cdot(s\hat{\mathbf{x}}+\mathbf{R})} c_{s\hat{\mathbf{x}}+\mathbf{R},\sigma}, \tag{A1}$$

the on-site interaction Hamiltonian is

$$H_U = U \sum_{\mathbf{k},\mathbf{p},\mathbf{q}s\sigma} c^\dagger_{\mathbf{p}+\mathbf{q},s\sigma} c^\dagger_{-\mathbf{p}s,-\sigma} c_{-\mathbf{k}s,-\sigma} c_{\mathbf{k}+\mathbf{q},s\sigma}, \tag{A2}$$

while the nearest-neighbor interaction Hamiltonian is

$$H_V = 2V \sum_{\mathbf{k},\mathbf{p},\mathbf{q}s\sigma\sigma'} [\cos(p_y - k_y) c^\dagger_{\mathbf{p}+\mathbf{q},s\sigma} c^\dagger_{-\mathbf{p}s\sigma'} c_{-\mathbf{k}s\sigma'} c_{\mathbf{k}+\mathbf{q},s\sigma} + \cos(p_x - k_x) c^\dagger_{\mathbf{p}+\mathbf{q},s\sigma} c^\dagger_{-\mathbf{p},s+1,\sigma'} c_{-\mathbf{k},s+1,\sigma'} c_{\mathbf{k}+\mathbf{q},s\sigma}]. \tag{A3}$$

In the basis Eq. (2), the operators $c_{\mathbf{k}s}$ are

$$c_{\mathbf{k}s} = \frac{1}{\sqrt{2}} \left[(-1)^s \sqrt{1 - (-1)^s \frac{\cos k_y}{E(\mathbf{k})}} d_{\mathbf{k}+} + \sqrt{1 + (-1)^s \frac{\cos k_y}{E(\mathbf{k})}} d_{\mathbf{k}-} \right]. \tag{A4}$$

To project the interactions, we insert Eq. (A4) into the interaction Hamiltonian and restrict α to a single value for the desired band, i.e.,

$$c_{\mathbf{k}s} \to \frac{(-\alpha)^s}{\sqrt{2}} \sqrt{1 - \alpha(-1)^s \frac{\cos k_y}{E(\mathbf{k})}} d_{\mathbf{k}\alpha} \tag{A5}$$

and sum over s.

We are interested in the $\mathbf{q} = 0$ and $\mathbf{q} = \mathbf{Q} = \pi\hat{\mathbf{y}}$ cases corresponding to the $\ell_x = 0, 1$ pairing channels, which in the band basis are

$$H^{(\ell)}_{int,\alpha} = \sum_{\mathbf{k}\mathbf{p}\sigma\sigma'} g^{(\ell;\alpha)}(\mathbf{p};\mathbf{k}) d^\dagger_{\mathbf{p}+\ell\mathbf{Q},\alpha\sigma} d^\dagger_{-\mathbf{p}\alpha\sigma'} d_{-\mathbf{k}\alpha\sigma'} d_{\mathbf{k}+\ell\mathbf{Q},\alpha\sigma}. \tag{A6}$$

The relevant projections for $\ell_x = 0$ are

$$\begin{aligned} \sum_s c^\dagger_{\mathbf{p}s\sigma} c^\dagger_{-\mathbf{p}s\sigma'} c_{-\mathbf{k}s\sigma'} c_{\mathbf{k}s\sigma} &\to \frac{1}{4} \sum_s \left(1 - \alpha(-1)^s \frac{\cos p_y}{E(\mathbf{p})}\right)\left(1 - \alpha(-1)^s \frac{\cos k_y}{E(\mathbf{k})}\right) d^\dagger_{\mathbf{p}\alpha\sigma} d^\dagger_{-\mathbf{p}\alpha\sigma'} d_{-\mathbf{k}\alpha\sigma'} d_{\mathbf{k}\alpha\sigma} \\ &= \frac{1}{2}\left(1 + \frac{\cos p_y}{E(\mathbf{p})} \frac{\cos k_y}{E(\mathbf{k})}\right) d^\dagger_{\mathbf{p}\alpha\sigma} d^\dagger_{-\mathbf{p}\alpha\sigma'} d_{-\mathbf{k}\alpha\sigma'} d_{\mathbf{k}\alpha\sigma}, \end{aligned} \tag{A7}$$

$$\sum_s c^\dagger_{\mathbf{p}s\sigma} c^\dagger_{-\mathbf{p},s+1,\sigma'} c_{-\mathbf{k},s+1,\sigma'} c_{\mathbf{k}s\sigma} \to \frac{1}{4}\sum_s \sqrt{1-\frac{\cos^2 p_y}{E^2(\mathbf{p})}}\sqrt{1-\frac{\cos^2 k_y}{E^2(\mathbf{k})}} d^\dagger_{\mathbf{p}\alpha\sigma} d^\dagger_{-\mathbf{p}\alpha\sigma'} d_{-\mathbf{k}\alpha\sigma'} d_{\mathbf{k}\alpha\sigma}$$
$$= \frac{1}{2}\frac{\cos p_x}{E(\mathbf{p})}\frac{\cos k_x}{E(\mathbf{k})} d^\dagger_{\mathbf{p}\alpha\sigma} d^\dagger_{-\mathbf{p}\alpha\sigma'} d_{-\mathbf{k}\alpha\sigma'} d_{\mathbf{k}\alpha\sigma}. \tag{A8}$$

For $\ell_x = 1$, the projections are

$$\sum_s c^\dagger_{\mathbf{p}+\mathbf{Q},s\sigma} c^\dagger_{-\mathbf{p}s\sigma'} c_{-\mathbf{k}s\sigma'} c_{\mathbf{k}+\mathbf{Q},s\sigma} \to \frac{1}{4}\sum_s \sqrt{1-\frac{\cos^2 p_y}{E^2(\mathbf{p})}}\sqrt{1-\frac{\cos^2 k_y}{E^2(\mathbf{k})}} d^\dagger_{\mathbf{p}\alpha\sigma} d^\dagger_{-\mathbf{p}\alpha\sigma'} d_{-\mathbf{k}\alpha\sigma'} d_{\mathbf{k}\alpha\sigma}$$
$$= \frac{1}{2}\frac{|\cos p_x|}{E(\mathbf{p})}\frac{|\cos k_x|}{E(\mathbf{k})} d^\dagger_{\mathbf{p}\alpha\sigma} d^\dagger_{-\mathbf{p}\alpha\sigma'} d_{-\mathbf{k}\alpha\sigma'} d_{\mathbf{k}\alpha\sigma}, \tag{A9}$$
$$\sum_s c^\dagger_{\mathbf{p}+\mathbf{Q},s\sigma} c^\dagger_{-\mathbf{p},s+1,\sigma'} c_{-\mathbf{k},s+1,\sigma'} c_{\mathbf{k}+\mathbf{Q},s\sigma} \to \frac{1}{4}\sum_s \left(1+\alpha(-1)^s\frac{\cos p_y}{E(\mathbf{p})}\right)\left(1+\alpha(-1)^s\frac{\cos k_y}{E(\mathbf{k})}\right) d^\dagger_{\mathbf{p}\alpha\sigma} d^\dagger_{-\mathbf{p}\alpha\sigma'} d_{-\mathbf{k}\alpha\sigma'} d_{\mathbf{k}\alpha\sigma}$$
$$= \frac{1}{2}\left(1+\frac{\cos p_y}{E(\mathbf{p})}\frac{\cos k_y}{E(\mathbf{k})}\right) d^\dagger_{\mathbf{p}\alpha\sigma} d^\dagger_{-\mathbf{p}\alpha\sigma'} d_{-\mathbf{k}\alpha\sigma'} d_{\mathbf{k}\alpha\sigma}. \tag{A10}$$

Note that none of the form factors depend on the band index α, which we therefore drop from now on.

Next, we switch from the charge and spin decomposition of the interactions to the singlet and triplet pairing decomposition using the Pauli matrix completeness relation

$$2\delta_{\sigma_1\sigma_2'}\delta_{\sigma_1'\sigma_2} = \sum_\nu \sigma^\nu_{\sigma_1\sigma_1'}\sigma^\nu_{\sigma_2\sigma_2'} = \sum_\nu (\sigma^\nu i\sigma^y)^*_{\sigma_1\sigma_1'}(\sigma^\nu i\sigma^y)_{\sigma_2\sigma_2'}, \tag{A11}$$

where $\nu = 0, x, y, z$ with 0 corresponding to singlet and the rest to triplet pairing channels; this puts the projected interactions into the following form:

$$H^{(\ell_x\nu)}_{\text{int}} = \frac{1}{2}\sum_{\mathbf{k}\mathbf{p}\sigma_1\sigma_1'\sigma_2\sigma_2'} g^{(\ell_x\nu)}(\mathbf{p};\mathbf{k})(\sigma^\nu i\sigma^y)^*_{\sigma_1\sigma_1'}(\sigma^\nu i\sigma^y)_{\sigma_2\sigma_2'} d^\dagger_{\mathbf{p}+\ell_x\mathbf{Q},\alpha\sigma_1} d^\dagger_{-\mathbf{p}\alpha\sigma_1'} d_{-\mathbf{k}\alpha\sigma_2} d_{\mathbf{k}+\ell_x\mathbf{Q},\alpha\sigma_2'}. \tag{A12}$$

The anticommutation relations then imply

$$g^{(\ell_x\nu)}(\mathbf{p};\mathbf{k}) = (-1)^\nu g^{(\ell_x\nu)}(-\mathbf{p}-\ell_x\mathbf{Q};\mathbf{k}) = g^{(\ell_x\nu)}(-\mathbf{p}-\ell_x\mathbf{Q};-\mathbf{k}-\ell_\mathbf{x}\mathbf{Q}) \tag{A13}$$

[with $(-1)^\nu = -1$ for $\nu = x, y, z$], which implies that $g^{(\ell_x\nu)}(\mathbf{p};\mathbf{k})$ is even or odd under $\mathbf{p} \to -\mathbf{p}+\ell_x\mathbf{Q}$ for singlet and triplet channels, respectively.

We further split the projected interactions into $g^{(\ell_x\ell_y\nu)}(\mathbf{p};\mathbf{k}) = (-1)^{\ell_y} g^{(\ell_x\ell_y\nu)}(\mathbf{p}+\mathbf{Q};\mathbf{k})$ according to channels even and odd under $\hat{T}_x$, which we know from the irrep analysis must decouple. Finally, the $(00s)$ channel splits into a $\hat{C}_4$ even and odd parts (i.e., "s-" and "d-wave" channels) that we refer to as $(00s;s)$ and $(00s;d)$. The $\hat{C}_4$ symmetry acts as

$$\hat{C}_4 c_{\mathbf{p}+\ell_x\mathbf{Q},s\sigma}\hat{C}_4^\dagger = \frac{1}{2}\sum_{s'\ell_x'}(-1)^{ss'+\ell_x s'+\ell_x' s} c_{\bar{\mathbf{p}}+\ell_x'\mathbf{Q},s'\sigma}. \tag{A14}$$

Using the fact that $\cos(p_j - k_j) = \cos p_j \cos k_j + \sin p_j \sin k_j$, we find that the projected interactions for each channel are

$$g^{(00s;s)}(\mathbf{p};\mathbf{k}) = \frac{U}{2} + V\frac{(\cos^2 p_y + \cos^2 p_x)(\cos^2 k_y + \cos^2 k_x)}{E(\mathbf{p})E(\mathbf{k})},$$
$$g^{(00s;d)}(\mathbf{p};\mathbf{k}) = V\frac{(\cos^2 p_y - \cos^2 p_x)(\cos^2 k_y - \cos^2 k_x)}{E(\mathbf{p})E(\mathbf{k})},$$
$$g^{(01s)}(\mathbf{p};\mathbf{k}) = \frac{U}{2}\frac{\cos p_y \cos k_y}{E(\mathbf{p})E(\mathbf{k})} + V\cos p_y \cos k_y,$$
$$g^{(10s)}(\mathbf{p};\mathbf{k}) = \frac{U}{2}\frac{\cos p_x \cos k_x}{E(\mathbf{p})E(\mathbf{k})} + V\cos p_x \cos k_x,$$
$$g^{(11s)}(\mathbf{p};\mathbf{k}) = V\frac{\sin p_y \cos p_x \sin k_y \cos k_x}{E(\mathbf{p})E(\mathbf{k})} + V\frac{\sin p_x \cos p_y \sin k_x \cos k_y}{E(\mathbf{p})E(\mathbf{k})}, \tag{A15}$$
$$g^{(00t)}(\mathbf{p};\mathbf{k}) = V\frac{\sin p_y \cos p_y \sin k_y \cos k_y}{E(\mathbf{p})E(\mathbf{k})} + V\frac{\sin p_x \cos p_x \sin k_x \cos k_x}{E(\mathbf{p})E(\mathbf{k})},$$
$$g^{(01t)}(\mathbf{p};\mathbf{k}) = V\sin p_y \sin k_y,$$
$$g^{(10t)}(\mathbf{p};\mathbf{k}) = V\sin p_x \sin k_x,$$
$$g^{(11t)}(\mathbf{p};\mathbf{k}) = V\frac{\cos p_x \cos p_y \cos k_x \cos k_y}{E(\mathbf{p})E(\mathbf{k})}.$$

From these we obtain Table I. Observe that $\pi\hat{\mathbf{y}}$ and $\pi\hat{\mathbf{x}}$ are mapped to each other by $\hat{C}_4$ (since it exchanged $\hat{T}_x$ and $\hat{T}_y$), which implies that (01ν) and (10ν) channels form two components of the same space group irrep; the little point group is trivial in this case since $\hat{C}_4$ symmetry is broken. The irreps of (00ν) and (11ν), on the other hand, have a trivial star but a nontrivial little point group, and are therefore classified according to the irreps of D_{4h} (since inversion symmetry is also present). In particular, the $(00s;s)$ channel corresponds to the trivial irrep A_{1g}, $(00s;d)$ to the B_{1g} irrep, $(11s)$ to the E_g irrep, $(00t)$ to the E_u irrep, and $(11t)$ to the A_{1u} irrep.

An astute reader may notice that the $g^{(10\nu)}$ and $g^{(11\nu)}$ are discontinuous on the MBZ due to factors of $\cos k_x$, which evaluate to ± 1 for $k_x = \pm\pi/2$, respectively, on the MBZ boundary. However, this is only an apparent discontinuity that is due to the discontinuity of the $d_{\mathbf{k}\alpha}$, a consequence of the presence of Dirac nodes in the system that imply an existence of a branch cut in the wave function. Note in particular that the operator $c_{\mathbf{k}1}$ has a branch cut at the $k_x = \pm\pi/2$ because, as follows from the definition in Eq. (A1),

$$c_{\mathbf{k}+\pi\hat{\mathbf{x}},s} = e^{-ik_x s} c_{\mathbf{k}s}, \tag{A16}$$

so that technically $c_{(\pi/2,k_y),1} = -c_{(-\pi/2,k_y),1}$. For that reason we need to consider $k_x = \pi/2$ and $k_x = -\pi/2$ as distinct points. The operators $d_{\mathbf{k}\alpha}$ can be made continuous for $\alpha \cos k_y < 0$ if we take

$$d_{\mathbf{k}\alpha} = \frac{1}{\sqrt{2}}\sqrt{1+\alpha\frac{\cos k_y}{E(\mathbf{k})}}c_{\mathbf{k}0} + \frac{\alpha\,\mathrm{sgn}[\cos k_x]}{\sqrt{2}}\sqrt{1-\alpha\frac{\cos k_y}{E(\mathbf{k})}}c_{\mathbf{k}1}, \tag{A17}$$

so that $d_{\mathbf{k}+\pi\hat{\mathbf{x}},\alpha} = d_{\mathbf{k}\alpha}$ for $\alpha\cos k_y < 0$. For $\alpha\cos k_y > 0$, however, we then get

$$\begin{aligned} d_{(\pi/2,k_y)\alpha} &= \alpha\,\mathrm{sgn}[\cos(\pi/2)]c_{(\pi/2,k_y)1} \\ &= -\alpha\,\mathrm{sgn}[\cos(\pi/2)]c_{(-\pi/2,k_y)1} \\ &= -\frac{\mathrm{sgn}[\cos(\pi/2)]}{\mathrm{sgn}[\cos(-\pi/2)]}d_{(-\pi/2,k_y)\alpha}. \end{aligned}$$

To be consistent, one is forced to take $d_{(\pi/2,k_y)\alpha} = -d_{(-\pi/2,k_y)\alpha}$ for $\alpha\cos k_y > 0$, with the coefficients in Eq. (A17) being continuous.

Taking this into account, we note that, while anticommutation relations typically imply that triplet interaction must vanish when $\mathbf{p} = -\mathbf{p} + \ell_{\mathbf{x}}\mathbf{Q}$, one has to be careful in the case $p_x = \pm\pi/2$ because of the fact that $d_{(\pi/2,k_y)\alpha} = -d_{(-\pi/2,k_y)\alpha}$ for $\alpha\cos k_y > 0$. This makes no difference for $\ell_x = 0$ since the minus signs cancel, but for $\ell_x = 1$ there is an additional minus sign that means that

$$g^{(1\nu)}((\pi/2,k_y);\mathbf{k}) = -(-1)^{\nu} g^{(1\nu)}((\pi/2,k_y);\mathbf{k}), \tag{A18}$$

i.e., it is the singlet projected interactions that must vanish while the triplet interaction does not, consistent with our results.

APPENDIX B: SOME DETAILS OF THE GAP EQUATION

Here we provide a few details about solving the gap equation (9). In most cases, there is a single component $m = 0$, and we simply evaluate the integral on the right-hand side (RHS). The only nontrivial cases are for the $(00s;s)$, $(01s)$, and $(10s)$ channels, for which the reduced gap equation becomes a 2×2 matrix equation admitting two solutions in each channel. In particular, for the $(00s;s)$ channel we have

$$\begin{pmatrix} D_0^{(00s;s)} \\ D_1^{(00s;s)} \end{pmatrix} = -\begin{pmatrix} U\tilde{\Pi}_{00}^{(00s;s)}/2 & U\tilde{\Pi}_{01}^{(00s;s)}/2 \\ V\tilde{\Pi}_{01}^{(00s;s)} & V\tilde{\Pi}_{11}^{(00s;s)} \end{pmatrix}\begin{pmatrix} D_0^{(00s;s)} \\ D_1^{(00s;s)} \end{pmatrix}. \tag{B1}$$

The matrix has eigenvalues

$$\gamma_{\pm}^{(00s;s)} = \frac{1}{4}\left[U\tilde{\Pi}_{00}^{(00s;s)} + 2V\tilde{\Pi}_{11}^{(00s;s)} \mp \sqrt{\left(U\tilde{\Pi}_{00}^{(00s;s)} - 2V\tilde{\Pi}_{11}^{(00s;s)}\right)^2 + 8UV\left(\tilde{\Pi}_{01}^{(00s;s)}\right)^2}\right], \tag{B2}$$

with eigenstates that determine the relative weights of $D_0^{(00s;s)}$ and $D_1^{(00s;s)}$:

$$\begin{pmatrix} D_{0,\pm}^{(00s;s)} \\ D_{1,\pm}^{(00s;s)} \end{pmatrix} \propto \begin{pmatrix} U\tilde{\Pi}_{00}^{(00s;s)} + 2V\tilde{\Pi}_{11}^{(00s;s)} \mp \sqrt{\left(U\tilde{\Pi}_{00}^{(00s;s)} - 2V\tilde{\Pi}_{11}^{(00s;s)}\right)^2 + 8UV\left(\tilde{\Pi}_{01}^{(00s;s)}\right)^2} \\ 4V\tilde{\Pi}_{01}^{(00s;s)} \end{pmatrix} \tag{B3}$$

(note that the linearized gap equation does not fix the magnitude of the $D_m^{(\ell_x\ell_y\nu)}$ coefficients). The equations are similar for the $(01s)$ and $(10s)$ channels, which are degenerate because they belong to the same space group irrep.

In the end we thus obtain the self-consistency relations

$$1 = -\gamma^{(\ell_x\ell_y\nu)}(T), \tag{B4}$$

which is an equation for T_c since the RHS is a function of temperature T. At the phase transition, the instability happens only for the channels with the highest T_c, and we can ignore the rest. In particular, since $\gamma_+^{(00s;s)} < \gamma_-^{(00s;s)}$, the $\gamma_-^{(00s;s)}$ channel always gives a lower T_c and it can be ignored; we thus only keep the $+$ solution and can drop the $\pm$ index. To obtain the mean-field phase diagram, we select the channel with largest eigenvalue (numerically we observe that which eigenvalue is largest appears to be independent of the temperature).

APPENDIX C: FOURTH-ORDER FREE ENERGY

When the winning irrep is 2D, in order to determine the symmetries of the ground state it is necessary to go to the

fourth order in the free energy. The Ginzburg-Landau free energy for Hofstadter superconductors with arbitrary flux has been derived in Ref. [33], here we summarize the simplified case for π flux. Defining the matrix gap function $\hat{\Delta}(\mathbf{p})$ via

$$H_{SC} = \sum \hat{\Delta}_{\ell\ell';\sigma\sigma'}(\mathbf{p}) d^{\dagger}_{\mathbf{p},\ell,\sigma} d^{\dagger}_{\mathbf{p},\ell,\sigma'}, \tag{C1}$$

with $\mathbf{p}$ restricted to the reduced MBZ, the fourth-order term in the free energy can be computed as

$$\mathcal{F}^{(4)} = \sum_{\mathbf{k}} \beta(\mathbf{p}) \mathrm{Tr}[\hat{\Delta}^{\dagger}(\mathbf{p})\hat{\Delta}(\mathbf{p})\hat{\Delta}^{\dagger}(\mathbf{p})\hat{\Delta}(\mathbf{p})], \tag{C2}$$

with the trace taken over both the magnetic patch indices and the spin indices, and where

$$\beta(\mathbf{p}) = \sum_n \frac{1}{\left[\omega_n^2 + \epsilon^2(\mathbf{p})\right]^2} = \frac{T \tanh\left(\frac{\epsilon}{2T}\right) - \epsilon \mathrm{sech}^2\left(\frac{\epsilon}{2T}\right)}{8\epsilon^3 T^2}. \tag{C3}$$

Note that, in the case of interest (for the $\mathbf{Q}_t^*$ triplet PDW irrep),

$$\hat{\Delta} = \begin{pmatrix} \Delta^{(01)}(\mathbf{p}) & \Delta^{(10)}(\mathbf{p}) \\ \Delta^{(10)}(\mathbf{p}) & -\Delta^{(01)}(\mathbf{p}) \end{pmatrix}, \tag{C4}$$

and the trace evaluates to

$$\mathrm{Tr}[\hat{\Delta}^{\dagger}(\mathbf{p})\hat{\Delta}(\mathbf{p})\hat{\Delta}^{\dagger}(\mathbf{p})\hat{\Delta}(\mathbf{p})] = \tfrac{1}{4}[(|\Delta^{(01)}|^2 + |\Delta^{(10)}|^2)^2 + 2|\Delta^{(01)}|^2|\Delta^{(10)}|^2 - ((\Delta^{(01)})^2(\Delta^{(10)*})^2 + \mathrm{c.c.})] \tag{C5}$$

After the sum over momentum, the free energy is written in terms of the order parameters $D^{(\ell,\pm)}$ in Eq. (8) as

$$\mathcal{F}^{(4)} = \beta_0\left(|D^{(01)}|^2 + |D^{(10)}|^2\right)^2 + 2\beta_1|D^{(01)}|^2|D^{(10)}|^2 - \beta_1\left(\left(D^{(01)}\right)^2\left(D^{(10)*}\right)^2 + \mathrm{c.c.}\right). \tag{C6}$$

The minimum of the free energy is degenerate between unidirectional combinations in which only one of $D^{(01)}$ or $D^{(10)}$ is nonzero (breaking TRS and $\hat{C}_4$ symmetry), and bidirectional combinations where $D^{(01)} = \pm D^{(10)}$. Additional terms neglected in our model may favor unidirectional or bidirectional combinations.

APPENDIX D: DETAILS OF RENORMALIZATION-GROUP CALCULATION

We use the RG flow equations we derived in Ref. [44] (see Supplemental Material of that reference), which we reproduce here for the special case of the π-flux lattice. In the patch RG formalism we consider states close to the VHS points $\mathbf{K}_{\ell_x,\mathrm{v}} = ((1+\mathrm{v})\frac{\pi}{2}, \mathrm{v}\frac{\pi}{2}) + \ell_x\mathbf{Q}$ where we introduce the VHS index $\mathrm{v} = 0, 1$ (for simplicity we set $\ell_x = \ell$ defined modulo two and we omit the subscript). Corresponding to these states we define operators $d_{\mathbf{p}\ell\mathrm{v}\alpha\sigma} = d_{\mathbf{p}+\mathbf{K}_{\ell,\mathrm{v}},\alpha,\sigma}$ with $\mathbf{p}$ being a small momentum expanded around a patch centered at $\mathbf{K}_{\ell,\mathrm{v}}$. For bookkeeping purposes it will also be convenient to introduce a redundant VHS index $\mathrm{v} = -1$, with $\mathbf{K}_{\ell,-1} = \mathbf{K}_{\ell-1,1}$. We similarly consider the interactions in the vicinity of these patches:

$$H_{\mathrm{int}} \to \frac{1}{2} \sum_{\substack{\ell mn \\ \mathrm{uvw},\sigma\sigma'}} g^{(\ell,\mathrm{u})}_{m,\mathrm{v};n,\mathrm{w}} d^{\dagger}_{\ell+n,\mathrm{u}+\mathrm{w},\alpha,\sigma} d^{\dagger}_{-n,-\mathrm{w},\alpha,\sigma'} \times d_{-m,-\mathrm{v},\alpha,\sigma'} d_{\ell+m,\mathrm{u}+\mathrm{v},\alpha,\sigma}, \tag{D1}$$

where $\ell, m, n = 0, 1$ are magnetic flavor indices, $\mathrm{u}, \mathrm{v}, \mathrm{w} = 0, \pm 1$ are additional VHS indices.

In the pairing channel we have $g^{(\ell,0)}_{m,\mathrm{v};n,\mathrm{w}} = g^{(\ell;\alpha)}(\mathbf{K}_{m,\mathrm{v}}; \mathbf{K}_{n,\mathrm{w}})$, and there are additional $g^{(\ell,1)}_{m,\mathrm{v};n,\mathrm{w}}$ interactions in the particle-hole channel corresponding to interactions between pairs with total momentum $(\pi/2, \pi/2) + \ell\mathbf{Q}$. We group the interactions according to their VHS indices as follows:

$$\begin{aligned} g^{(\ell)1}_{mn} &= g^{(\ell,0)}_{m,0;n,0}, & g^{(\ell)1'}_{mn} &= g^{(\ell,0)}_{m,1;n,1}, \\ g^{(\ell)2}_{mn} &= g^{(\ell,1)}_{m,0;n,0}, & g^{(\ell)3}_{mn} &= g^{(\ell,1)}_{m,0;n,-1}, \\ g^{(\ell)4}_{mn} &= g^{(\ell,0)}_{m,0;n,1}, \end{aligned} \tag{D2}$$

The corresponding Feynman diagrams are shown in Fig. 4. Note that some of the diagrams are redundant due to Hermiticity and commutation relations. In particular,

$$\begin{aligned} g^{(\ell)1}_{mn} &= g^{(\ell),1*}_{nm} = g^{(\ell)1}_{-\ell-m,-\ell-n}, \\ g^{(\ell)1'}_{mn} &= g^{(\ell),1'*}_{nm} = g^{(\ell)1'}_{-1-\ell-m,-1-\ell-n}, \\ g^{(\ell)2}_{mn} &= g^{(\ell),2*}_{nm} = g^{(\ell)2'}_{-\ell-m,-\ell-n}, \\ g^{(\ell)3}_{mn} &= g^{(\ell),3*}_{-\ell-n,-\ell-m} = g^{(\ell)3'}_{-\ell-m,-\ell-n}, \\ g^{(\ell)4}_{mn} &= g^{(\ell),4}_{-\ell-m,-\ell-n-1} = g^{(\ell)4'*}_{nm}. \end{aligned} \tag{D3}$$

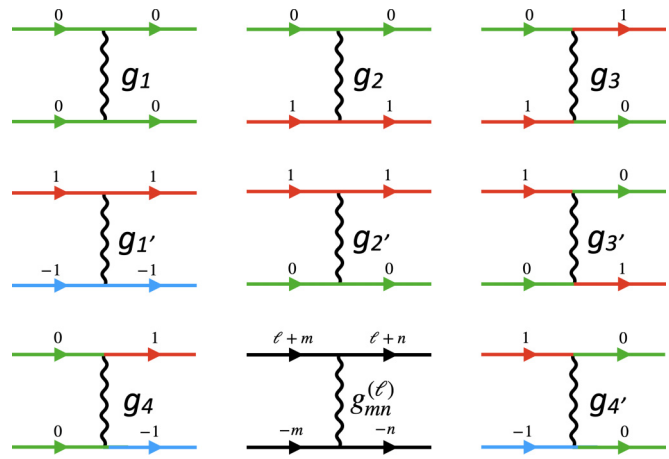

FIG. 4. Feynman diagrams corresponding to interactions in Eq. (D1). The colors indicate the VHS indices for the intrapatch processes g_j (green lines correspond to $\mathrm{v} = 0$, red to $\mathrm{v} = 1$ and blue to $\mathrm{v} = -1$). The colorless diagram shows the interpatch indices with ℓ labeling the total momentum of the incoming and outgoing pairs, and m and n labeling the relative momenta of incoming and outgoing pairs, respectively.

These are in addition to the MTG-imposed relation $g^{(\ell),j}_{mn} = g^{(\ell),j}_{m-1,n-1}$ and TRS that implies that all coupling constants are real, so that in total there are 16 independent coupling constants.

The basic building blocks of RG are the particle-particle bubble, which also serves as the RG time $t = \Pi^{(0)}_{pp}$,

$$\Pi^{(\mathrm{v})}_{pp} = -iT\sum_{\omega}\int G_{n,\mathrm{v}}(i\omega,\mathbf{p})G_{\ell-n,\mathrm{v}}(-i\omega,-\mathbf{p})\frac{d^2p}{(2\pi)^2} = \nu_0\log^2\frac{\Lambda}{E}, \tag{D4}$$

and the particle-hole bubble is

$$\Pi^{(\mathrm{v})}_{ph} = iT\sum_{\omega}\int G_{n,\mathrm{v}}(i\omega,\mathbf{p})G_{\ell+n,\mathrm{v}+1}(i\omega,\mathbf{p})\frac{d^2p}{(2\pi)^2} = \nu_0\log^2\frac{\Lambda}{E} \tag{D5}$$

(neither of the bubbles depends on the choice of n and ℓ by MTG symmetry), where

$$G_{n,\mathrm{v}}(i\omega,\mathbf{p}) = \frac{1}{i\omega-\varepsilon_{n,\mathrm{v}}(\mathbf{p})} \tag{D6}$$

is the Green's function for the patch around $\mathbf{K}_{n,\mathrm{v}}$, and E is the energy scale down to which the high-energy modes have been integrated out to. The dispersion expanded around the VHS points is $\varepsilon_{\ell,\mathrm{v}}(\mathbf{p}) \approx \pm(-1)^{\mathrm{v}}\frac{p_x^2-p_y^2}{2m} - \mu$ (with $\pm$ for upper and lower bands), and the extra logarithm comes from the diverging DOS at the VHSs. We further define $d^{(\mathrm{v})}_{pp} = d\Pi^{(\mathrm{v})}_{pp}/d\Pi^{(0)}_{pp} \approx \Pi^{(\mathrm{v})}_{pp}/\Pi^{(0)}_{pp}$ and $d^{(\mathrm{v})}_{ph} = d\Pi^{(\mathrm{v})}_{ph}/d\Pi^{(0)}_{pp} \approx \Pi^{(\mathrm{v})}_{ph}/\Pi^{(0)}_{pp}$. Note that due to the $\hat{C}_4$ symmetry $d^{(0)}_{pp} = d^{(1)}_{pp} = 1$ and $d^{(0)}_{ph} = d^{(1)}_{ph}$. We thus drop the superscripts.

We then obtain the standard 1-loop RG flow equation using the diagrams in Fig. 5, plugging in the magnetic flavor indices from Fig. 6, yielding the RG flow equations:

$$\begin{aligned}
\dot{g}^{(\ell)1}_{mn} &= -g^{(\ell)1}_{mk}g^{(\ell)1}_{kn} - g^{(\ell)4}_{mk}g^{(\ell)4*}_{nk},\\
\dot{g}^{(\ell)1'}_{mn} &= -g^{(\ell)1'}_{mk}g^{(\ell)1'}_{kn} - g^{(\ell)4*}_{km}g^{(\ell)4}_{kn},\\
\dot{g}^{(\ell)2}_{mn} &= d_{ph}\big(g^{(\ell+n-k)2}_{mk}g^{(\ell+m-k)2}_{kn} + g^{(\ell+n-k)4*}_{k,m-1}g^{(\ell+m-k)4}_{k,n-1}\big),\\
\dot{g}^{(\ell)3}_{mn} &= 2d_{ph}g^{(\ell+m+n+k)3}_{-n-k,-m-k}\big(g^{(k)2}_{m,-n-k} - g^{(k)3}_{mn}\big) + d_{ph}g^{(\ell+m+n+k)4}_{-n-k,-m-k}\big(g^{(k)4*}_{n,-m-k} - 2g^{(k)4*}_{n,m-1}\big) + d_{ph}g^{(\ell+m+n+k)4}_{-n-k,-n-\ell-1}g^{(k)4*}_{n,m-1},\\
\dot{g}^{(\ell)4}_{mn} &= -g^{(\ell)1}_{mk}g^{(\ell)4}_{kn} - g^{(\ell)4}_{mk}g^{(\ell)1'}_{kn} + d_{ph}\big(g^{(\ell+n-k)2}_{k-\ell-m-n,-\ell-n}g^{(\ell+m-k)4}_{kn} + g^{(\ell+n-k)4}_{mk}g^{(\ell+m-k-1)2}_{k+1,n+1}\big)\\
&\quad + d_{ph}g^{(\ell+m+n+k)4}_{-n-k,-m-k}\big(g^{(k-1)2}_{-m-k+1,n+1} - 2g^{(k-1)3}_{1-k-m,-k-n}\big) + d_{ph}g^{(\ell+m+n+k)4}_{-n-k,-n-\ell-1}g^{(k-1)3}_{1-k-m,-k-n}\\
&\quad + d_{ph}g^{(\ell+m+n+k)3}_{-n-k,-m-k}g^{(k)4}_{-m-k,n} + d_{ph}\big(g^{(\ell+m+n+k),2}_{-n-k,-n-\ell} - 2g^{(\ell+m+n+k)3}_{-n-k,-m-k}\big)g^{(k)4}_{mn}.
\end{aligned} \tag{D7}$$

We then study this flow equation with the bare coupling constants obtained from the projection as the initial condition.

1. Vertices

To determine which instability is realized under the RG flow, we study the flow of the associated susceptibilities and vertices. The relevant vertex Hamiltonians are

$$\begin{aligned}
H_{SC} &= \Delta^{(\ell)}_{m;\mathrm{v}}i\sigma^y_{\sigma\sigma'}d^{\dagger}_{\ell+m,\mathrm{v},\sigma}d^{\dagger}_{-m,-\mathrm{v},\sigma'} + \mathrm{H.c.},\\
H_{CDW} &= \rho^{[\ell]}_{m;\mathrm{v}}d^{\dagger}_{\ell+m,-\mathrm{v},\sigma}d_{m,1+\mathrm{v},\sigma},\\
H_{SDW} &= \mathbf{M}^{[\ell]}_{m;\mathrm{v}}\cdot\boldsymbol{\sigma}_{\sigma\sigma'}d^{\dagger}_{\ell+m,-\mathrm{v},\sigma}d_{m,1+\mathrm{v},\sigma'}
\end{aligned} \tag{D8}$$

(summation over the indices is implied). $\Delta^{(\ell)}_{m;\mathrm{v}} = \Delta^{(\ell)}(\mathbf{K}_{m,\mathrm{v}})$ is the SC or PDW vertex, while $\rho^{[\ell]}_{m;\mathrm{v}}$, and $\mathbf{M}^{[\ell]}_{m;\mathrm{v}}$ are the CDW, and SDW vertices with momentum transfers $(\pi,\pi)/q + \ell\mathbf{Q}$. We use the notation $M^{[\ell,j]}_{m;\mathrm{v}}$ to denote the jth component of $\mathbf{M}^{[\ell,j]}_{m;\mathrm{v}}$, including CDW as a special case with $j = 0$, $\rho^{[\ell]} = M^{[\ell,0]}$.

The vertex RG flow is obtained using the diagrams shown in Figs. 7 and 8, which yields

$$\begin{aligned}
\dot{\Delta}^{(\ell)}_{m;0} &= -g^{(\ell)1}_{nm}\Delta^{(\ell)}_{n;0} - g^{(\ell)4*}_{mn}\Delta^{(\ell)}_{n;1},\\
\dot{\Delta}^{(\ell)}_{m;1} &= -g^{(\ell)4}_{nm}\Delta^{(\ell)}_{n;0} - g^{(\ell)1'}_{nm}\Delta^{(\ell)}_{n;1},\\
\dot{\rho}^{[\ell]}_{m;0} &= d_{ph}\big(g^{(\ell+m-n)2}_{n-m,0} - 2g^{(\ell-m+n)3}_{0,-\ell}\big)\rho^{[\ell]}_{n;0}\\
&\quad + d_{ph}\big(g^{(\ell+m-n)4*}_{0,n-m-1} - 2g^{(\ell+m-n)4*}_{0,-\ell}\big)\rho^{[\ell]}_{n;1},\\
\dot{\rho}^{[\ell]}_{m;1} &= d_{ph}\big(g^{(\ell+m-n)4}_{n-m,-1} - 2g^{(\ell-m+n)4}_{0,-\ell}\big)\rho^{[\ell]}_{n;0}\\
&\quad + d_{ph}\big(g^{(\ell+m-n-1)2}_{1-\ell,1-\ell+n-m} - 2g^{(\ell+m-n-1)3}_{1-\ell,0}\big)\rho^{[\ell]}_{n;1},\\
\dot{M}^{[\ell]}_{m;0} &= d_{ph}\big(g^{(\ell+m-n)2}_{n-m,0}M^{[\ell]}_{n;0} + g^{(\ell+m-n)4*}_{0,n-m-1}M^{[\ell]}_{n;1}\big),\\
\dot{M}^{[\ell]}_{m;1} &= d_{ph}\big(g^{(\ell+m-n)4}_{n-m,-1}M^{[\ell]}_{n;0} + g^{(\ell+m-n-1)2}_{1-\ell,1-\ell+n-m}M^{[\ell]}_{n;1}\big).
\end{aligned} \tag{D9}$$

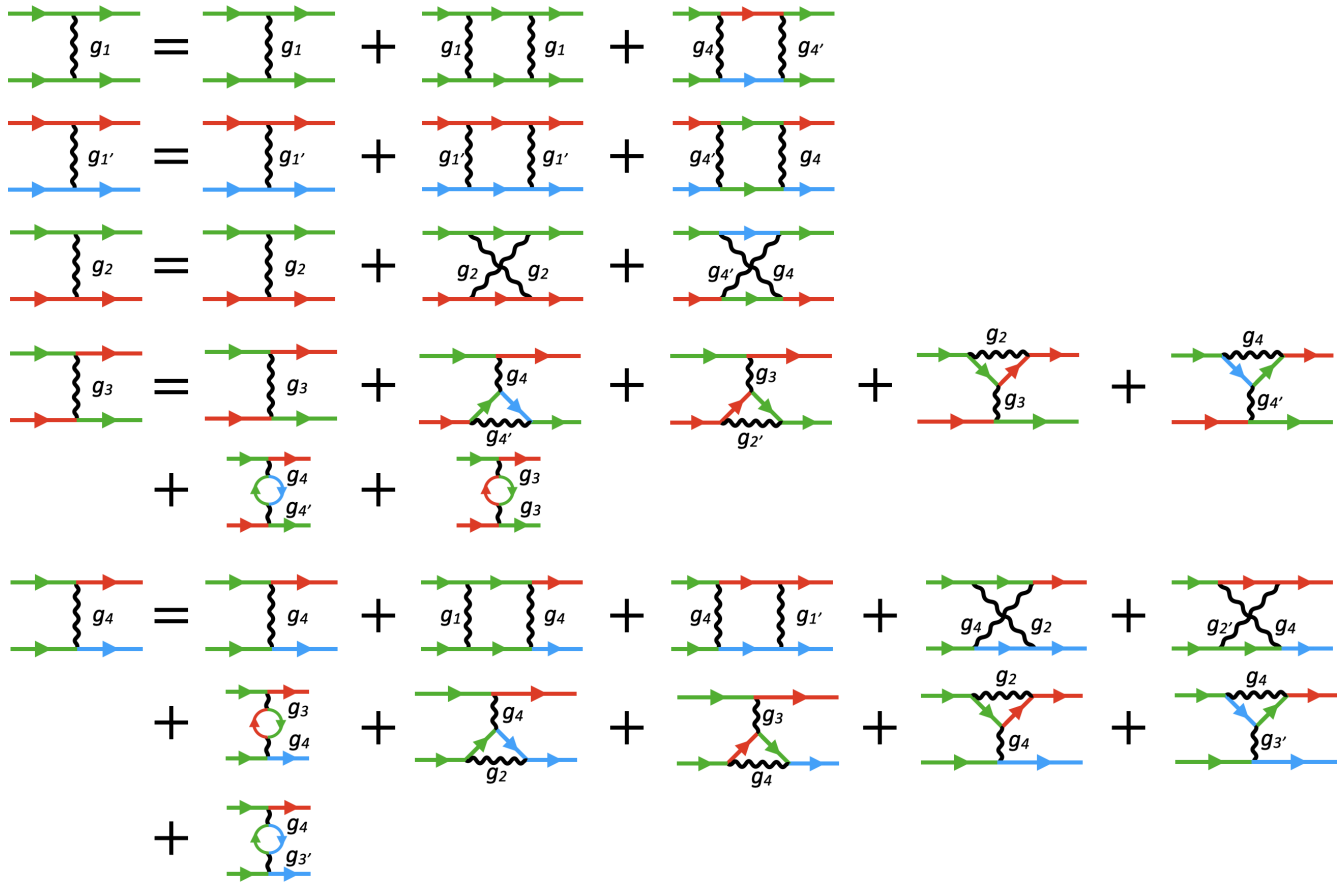

FIG. 5. The VHS index structure of the 1-loop RG flow diagrams.

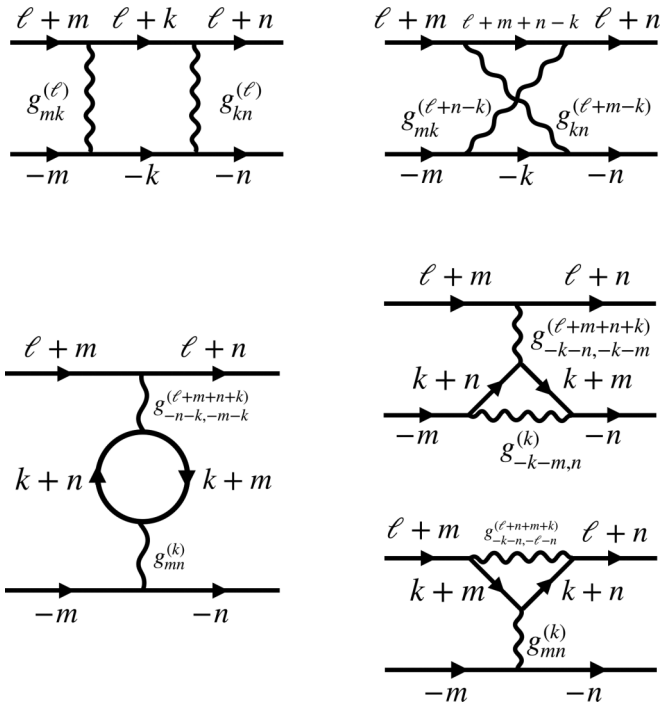

FIG. 6. Magnetic patch structure of 1-loop RG Feynman diagrams.

To identify the leading instability, we consider the susceptibilities χ_I with $I = \Delta^{(\ell)}_{m;\mathrm{v}}$, $\tilde{\rho}^{[\ell]}_{k;\mathrm{v}}$, $\tilde{M}^{[\ell]}_{k;\mathrm{v}}$. The susceptibilities flow as $\dot{\chi}_I = d_I |I(t)/I(0)|^2$ with $d_\Delta = 1$ and $d_I = d_{ph}$, and with $\chi_I(0) = 0$. The fastest diverging susceptibility corresponds to the leading instability. Solving the flow equations numerically we obtain the phase diagram Fig. 2(b). See Fig. 9 for a sample RG vertex flow. See Ref. [44] for additional details.

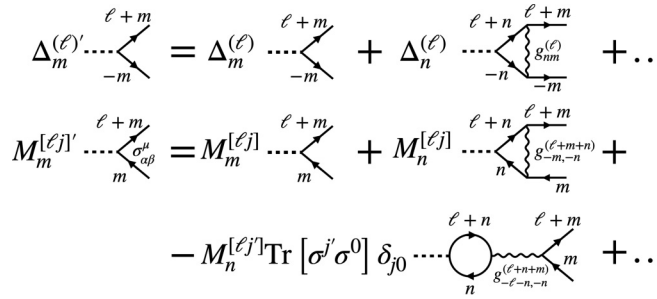

FIG. 7. Magnetic flavor structure of the 1-loop Feynman diagrams contributing to vertex flow.

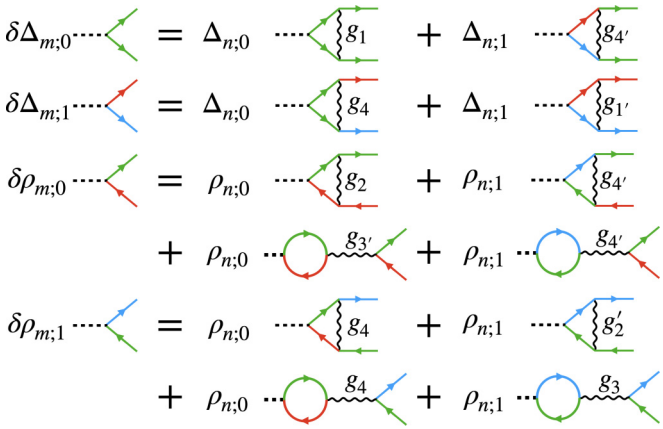

FIG. 8. VHS index structure of the 1-loop Feynman diagrams contributing to the vertex flow (green for v = 0, red or blue for v = ±1, respectively). SDW diagrams are the same as CDW diagrams with M instead of ρ.

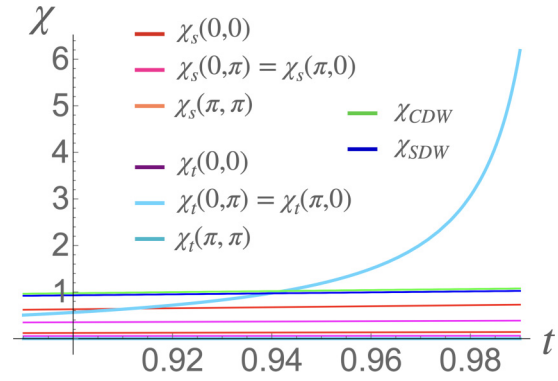

FIG. 9. Susceptibility RG flow for $U = 1$, $V = -0.5$, $d_{ph} = 1$. The triplet $\mathbf{Q}_t^*$ PDW with $(0, \pi)$ and $(0, \pi)$ (light blue curve) susceptibility diverges fastest. Other susceptibilities do not renormalize strongly on the relevant scale, indicating that the system is effectively described by the mean-field approximation.

[1] M. H. Hamidian, S. D. Edkins, S. H. Joo, A. Kostin, H. Eisaki, S. Uchida, M. J. Lawler, E. A. Kim, A. P. Mackenzie, K. Fujita, J. Lee, and J. C. S. Davis, Nature (London) **532**, 343 (2016).

[2] S. D. Edkins, A. Kostin, K. Fujita, A. P. Mackenzie, H. Eisaki, S. Uchida, S. Sachdev, M. J. Lawler, E.-A. Kim, J. C. Séamus Davis, and M. H. Hamidian, Science **364**, 976 (2019).

[3] X. Liu, Y. X. Chong, R. Sharma, and J. C. S. Davis, Science **372**, 1447 (2021).

[4] H. Chen, H. Yang, B. Hu, Z. Zhao, J. Yuan, Y. Xing, G. Qian, Z. Huang, G. Li, Y. Ye, S. Ma, S. Ni, H. Zhang, Q. Yin, C. Gong, Z. Tu, H. Lei, H. Tan, S. Zhou, C. Shen *et al.*, Nature (London) **599**, 222 (2021).

[5] A. Aishwarya, J. May-Mann, A. Raghavan, L. Nie, M. Romanelli, S. Ran, S. R. Saha, J. Paglione, N. P. Butch, E. Fradkin, and V. Madhavan, Nature **618**, 928 (2023).

[6] Q. Gu, J. P. Carroll, S. Wang, S. Ran, C. Broyles, H. Siddiquee, N. P. Butch, S. R. Saha, J. Paglione, J. C. S. Davis, and X. Liu, Nature **618**, 921 (2023).

[7] D. F. Agterberg, J. S. Davis, S. D. Edkins, E. Fradkin, D. J. Van Harlingen, S. A. Kivelson, P. A. Lee, L. Radzihovsky, J. M. Tranquada, and Y. Wang, Annu. Rev. Condens. Matter Phys. **11**, 231 (2020).

[8] O. Zachar, Phys. Rev. B **63**, 205104 (2001).

[9] N. J. Robinson, F. H. L. Essler, E. Jeckelmann, and A. M. Tsvelik, Phys. Rev. B **85**, 195103 (2012).

[10] A. Jaefari and E. Fradkin, Phys. Rev. B **85**, 035104 (2012).

[11] J. Venderley and E.-A. Kim, Sci. Adv. **5**, eaat4698 (2019).

[12] Y.-H. Zhang and A. Vishwanath, Phys. Rev. B **106**, 045103 (2022).

[13] K. S. Huang, Z. Han, S. A. Kivelson, and H. Yao, npj Quantum Mater. **7**, 17 (2022).

[14] F. Loder, S. Graser, A. P. Kampf, and T. Kopp, Phys. Rev. Lett. **107**, 187001 (2011).

[15] E. Berg, E. Fradkin, and S. A. Kivelson, Phys. Rev. B **79**, 064515 (2009).

[16] J. Kang and Z. Tešanović, Phys. Rev. B **83**, 020505 (2011).

[17] R. Soto-Garrido, G. Y. Cho, and E. Fradkin, Phys. Rev. B **91**, 195102 (2015).

[18] Y. Wang, D. F. Agterberg, and A. Chubukov, Phys. Rev. Lett. **114**, 197001 (2015).

[19] S.-K. Jian, Y.-F. Jiang, and H. Yao, Phys. Rev. Lett. **114**, 237001 (2015).

[20] R.-G. Cai, L. Li, Y.-Q. Wang, and J. Zaanen, Phys. Rev. Lett. **119**, 181601 (2017).

[21] M. Barkman, A. A. Zyuzin, and E. Babaev, Phys. Rev. B **99**, 220508(R) (2019).

[22] Y.-M. Wu, P. A. Nosov, A. A. Patel, and S. Raghu, Phys. Rev. Lett. **130**, 026001 (2023).

[23] P. A. Lee, Phys. Rev. X **4**, 031017 (2014).

[24] R. Soto-Garrido and E. Fradkin, Phys. Rev. B **89**, 165126 (2014).

[25] Y.-T. Hsu, A. Vaezi, M. H. Fischer, and E.-A. Kim, Nat. Commun. **8**, 14985 (2017).

[26] P. Coleman, A. Panigrahi, and A. Tsvelik, Phys. Rev. Lett. **129**, 177601 (2022).

[27] Y.-M. Wu, Z. Wu, and H. Yao, Phys. Rev. Lett. **130**, 126001 (2023).

[28] Z. Wu, Y.-M. Wu, and F. Wu, Phys. Rev. B **107**, 045122 (2023).

[29] J.-T. Jin, K. Jiang, H. Yao, and Y. Zhou, Phys. Rev. Lett. **129**, 167001 (2022).

[30] D. Shaffer, F. J. Burnell, and R. M. Fernandes, Phys. Rev. B **107**, 224516 (2023).

[31] D. R. Hofstadter, Phys. Rev. B **14**, 2239 (1976).

[32] D. Cocks, P. P. Orth, S. Rachel, M. Buchhold, K. Le Hur, and W. Hofstetter, Phys. Rev. Lett. **109**, 205303 (2012).

[33] D. Shaffer, J. Wang, and L. H. Santos, Phys. Rev. B **104**, 184501 (2021).

[34] I. Affleck and J. B. Marston, Phys. Rev. B **37**, 3774 (1988).

[35] P. W. Anderson, B. S. Shastry, and D. Hristopulos, Phys. Rev. B **40**, 8939 (1989).

[36] E. H. Lieb, Phys. Rev. Lett. **73**, 2158 (1994).

[37] A. W. W. Ludwig, M. P. A. Fisher, R. Shankar, and G. Grinstein, Phys. Rev. B **50**, 7526 (1994).

[38] X. G. Wen, F. Wilczek, and A. Zee, Phys. Rev. B **39**, 11413 (1989).
[39] T. Neupert, L. Santos, C. Chamon, and C. Mudry, Phys. Rev. Lett. **106**, 236804 (2011).
[40] T. Neupert, L. Santos, S. Ryu, C. Chamon, and C. Mudry, Phys. Rev. B **84**, 165107 (2011).
[41] H. Guo, E. Khatami, Y. Wang, T. P. Devereaux, R. R. P. Singh, and R. T. Scalettar, Phys. Rev. B **97**, 155146 (2018).
[42] Y.-X. Zhang, H.-M. Guo, and R. T. Scalettar, Phys. Rev. B **101**, 205139 (2020).
[43] D. J. Scalapino, Rev. Mod. Phys. **84**, 1383 (2012).
[44] D. Shaffer, J. Wang, and L. H. Santos, Nat. Commun. **13**, 7785 (2022).
[45] C. R. Dean, L. Wang, P. Maher, C. Forsythe, F. Ghahari, Y. Gao, J. Katoch, M. Ishigami, P. Moon, M. Koshino, T. Taniguchi, K. Watanabe, K. L. Shepard, J. Hone, and P. Kim, Nature (London) **497**, 598 (2013).
[46] L. A. Ponomarenko, R. V. Gorbachev, G. L. Yu, D. C. Elias, R. Jalil, A. A. Patel, A. Mishchenko, A. S. Mayorov, C. R. Woods, J. R. Wallbank, M. Mucha-Kruczynski, B. A. Piot, M. Potemski, I. V. Grigorieva, K. S. Novoselov, F. Guinea, V. I. Fal'ko, and A. K. Geim, Nature (London) **497**, 594 (2013).
[47] B. Hunt, J. D. Sanchez-Yamagishi, A. F. Young, M. Yankowitz, B. J. LeRoy, K. Watanabe, T. Taniguchi, P. Moon, M. Koshino, P. Jarillo-Herrero, and R. C. Ashoori, Science **340**, 1427 (2013).
[48] Y. Saito, J. Ge, L. Rademaker, K. Watanabe, T. Taniguchi, D. A. Abanin, and A. F. Young, Nat. Phys. **17**, 478 (2021).
[49] J. Yu, B. A. Foutty, Z. Han, M. E. Barber, Y. Schattner, K. Watanabe, T. Taniguchi, P. Phillips, Z.-X. Shen, S. A. Kivelson, and B. E. Feldman, Nat. Phys. **18**, 825 (2022).
[50] M. Aidelsburger, M. Atala, M. Lohse, J. T. Barreiro, B. Paredes, and I. Bloch, Phys. Rev. Lett. **111**, 185301 (2013).
[51] N. R. Cooper, J. Dalibard, and I. B. Spielman, Rev. Mod. Phys. **91**, 015005 (2019).
[52] P. Lauria, W.-T. Kuo, N. R. Cooper, and J. T. Barreiro, Phys. Rev. Lett. **128**, 245301 (2022).
[53] Y. Yu, L. Ma, P. Cai, R. Zhong, C. Ye, J. Shen, G. D. Gu, X. H. Chen, and Y. Zhang, Nature (London) **575**, 156 (2019).
[54] O. Can, T. Tummuru, R. P. Day, I. Elfimov, A. Damascelli, and M. Franz, Nat. Phys. **17**, 519 (2021).
[55] D. F. Agterberg, M. Sigrist, and H. Tsunetsugu, Phys. Rev. Lett. **102**, 207004 (2009).
[56] D. F. Agterberg and H. Tsunetsugu, Nat. Phys. **4**, 639 (2008).
[57] H. J. Schulz, Europhys. Lett. **4**, 609 (1987).
[58] I. E. Dzyaloshinskii, Zh. Eksp. Teor. Fiz. **93**, 1487 (1987) [Sov. Phys. JETP **66**, 848 (1987)].
[59] R. Nandkishore, L. S. Levitov, and A. V. Chubukov, Nat. Phys. **8**, 158 (2012).
[60] E. Fradkin, S. A. Kivelson, and J. M. Tranquada, Rev. Mod. Phys. **87**, 457 (2015).
[61] E. Berg, E. Fradkin, and S. A. Kivelson, Nat. Phys. **5**, 830 (2009).
[62] L. H. Santos, Y. Wang, and E. Fradkin, Phys. Rev. X **9**, 021047 (2019).